

Electrical resistivity, thermal conductivity, and viscosity of Fe-H alloys at Earth's core conditions

Cong Liu* and R. E. Cohen†

*Extreme Materials Initiative, Earth and Planets Laboratory, Carnegie Institution for Science,
5241 Broad Branch Road NW, Washington, District of Columbia 20015, USA*

The transport properties (electrical resistivity, thermal conductivity, and viscosity) of iron-hydrogen alloy are of great significance in the stability and evolution of planetary magnetic fields. Here, we investigate the thermal transport properties of iron doped with varying hydrogen content as functions of pressure (P) and temperature (T) for the top and bottom of Earth's outer core and beyond, corresponding to pressures of about 130 to 300 GPa and temperatures of 4000 to 7000 K. Using first-principles density functional theory molecular dynamic simulations (FPMD), we verify that crystalline FeH_x is superionic with H diffusing freely. We find a low frequency viscosity of 10-11 *mPa · s* for liquid Fe-H alloys at Earth's outer core conditions by the linear response Green-Kubo formula. Using the KKR method within density functional theory (DFT) plus Dynamical mean-field Theory (DMFT), we find saturation of electrical resistivity with increasing temperatures in liquid iron at outer core conditions. The effect of H on electrical and thermal transport we find is small, so that the exact H content of the core is not needed. The primary effect of H is on the equation of state, decreasing the density at constant P and T. We find the Lorenz number is smaller than the ideal value, and obtain for X(H)= 0.20, or 0.45 wt% H, thermal conductivity κ of ~ 105 and ~ 190 *Wm⁻¹K⁻¹*, respectively, at conditions near the core-mantle and inner-outer core boundary.

The Earth's core, primarily an iron-nickel alloy, has 5-10% lower density than pure iron at core conditions, suggesting the presence of lighter elements like hydrogen, carbon, oxygen, silicon, and sulfur[1, 2]. These elements may affect the core's physical and chemical properties, such as viscosity, electrical resistivity, and thermal conductivity, which are crucial for understanding the core's thermal evolution, geomagnetic field dynamics, and overall behavior of Earth's interior[3-5].

Challenging experimental studies have explored electrical and thermal transport in iron and its alloys as functions of pressure and temperature [5-9], but studying the effect of hydrogen on transport is exceedingly difficult experimentally because controlling and measuring small or variable hydrogen content in situ in the diamond anvil cell is very hard. Even for pure iron, there are significant variations in measured transport properties. For instance, direct measurements[5] of thermal conductivity under conditions close to those of Earth's core have yielded low values, such as 46 *Wm⁻¹K⁻¹*. These results support the conventional thermal dynamo theory and are consistent with a geodynamo driven by thermal convection throughout Earth's history. Other indirect measurements have given higher values (226 *Wm⁻¹K⁻¹*), as have estimates of thermal conductivity from electrical resistivity measurements in conjunction with the Wiedemann-Franz law [7], $\kappa = LT/\rho$, where thermal conductivity κ and electrical resistivity ρ are associated by temperature T and Lorenz number L, which is often estimated as the ideal low-temperature value, L_0 .

A number of density functional theory (DFT) based first-principles molecular dynamics [8, 10-12] and lin-

ear response computations [13] have also estimated iron transport properties. High values of thermal conductivity were computed using molecular dynamics [4], and earlier by first-principles linear response lattice dynamics. [13] These high values are inconsistent with the thermal convection mechanism in the core, suggesting the need for an alternative mechanism to explain the geodynamo[14, 15]. Recent theoretical calculations suggest a moderate thermal conductivity of approximately 100 ± 10 *Wm⁻¹K⁻¹* of hexagonal close-packed (*hcp*) Fe under core-mantle boundary (CMB) conditions with both electron-phonon (*e-ph*) and electron-electron (*e-e*) scattering contributions[16].

Previous research indicates that introducing light elements can significantly influence the transport properties, elastic wave velocities, and viscosity of Earth's interior[10, 17-21]. Given that hydrogen is the most abundant in the universe, it plays a pivotal role in the Earth's mantle and core. Understanding the effects of an iron-hydrogen alloy under core conditions is particularly intriguing. The superionic behavior[22-27] in the mantle suggests that hydrogen, when incorporated into iron under extreme pressure and temperature, could lead to unique transport properties. This includes potentially altered electrical and thermal conductivities, which are critical for modeling the core's thermal evolution and geomagnetic field dynamics. Additionally, the viscosity of the core, which influences convective processes and the geodynamo mechanism, could be markedly affected by the presence of hydrogen.

We performed first-principles molecular dynamics (FPMD) simulations with both VASP[28] and Quantum ESPRESSO[29] for Fe-H alloys at two fixed volumes per supercell (1071 and 905 \AA^3), representing the outermost and innermost outer core conditions, respectively (Fig. 1). A periodic hexagonal supercell containing 128

* Corresponding author: cliu10@carnegiescience.edu

† Corresponding author: rcohen@carnegiescience.edu

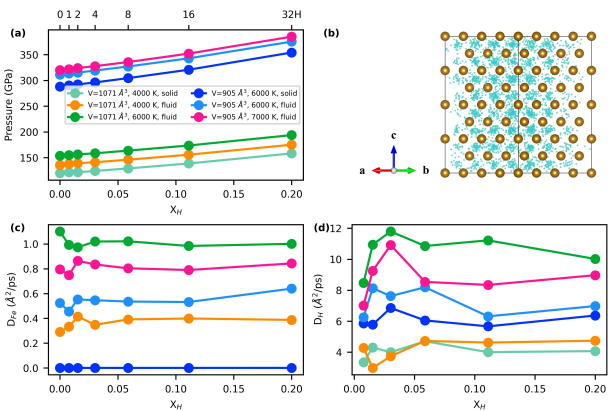


FIG. 1. **First-principles molecular dynamics simulations for iron-hydrogen alloy at Earth’s core conditions.** **a** Effects of hydrogen content on pressure at constant volume and temperature. Six curves are divided into two sets: solid at 4000 K (light green), fluid at 4000 K (orange), fluid at 6000 K (green) at larger volume ($V=1071 \text{ \AA}^3$ per supercell of 128 iron atoms); and solid at 6000 K (blue), fluid at 6000 K (light blue), and fluid at 7000 K (magenta) at smaller volume ($V=905 \text{ \AA}^3$ per same). **b** MD trajectory of solid $\text{Fe}_{128}\text{H}_{32}$ at 6000 K and $V=905 \text{ \AA}^3$. Brown and cyan atoms represent iron and hydrogen, respectively. Chemical diffusivities of **c** Fe and **d** H are derived from the slope of $\langle r^2(t) \rangle$. The top axes labels indicate the number of H in the 128 Fe supercell.

iron atoms was doped with varying amounts of hydrogen (0, 1, 2, 4, 8, 16, 32 H atoms, equal to 0-0.45 wt%) at interstitial sites. See Supplemental Material for computational details [30]. In our fixed cell simulations, we observed a linear increase in thermal pressure with the addition of hydrogen doping (Fig.1 a). This trend indicates that hydrogen incorporation into the iron lattice contributes significantly to the internal pressure. Hydrogen increases the pressure at constant volume, or increases the volume and decreases the density at constant pressure. In the solid phases, we found that hydrogen atoms can move freely within the iron *hcp* lattice (Fig.1 b), which is the so-called superionic state[31, 32].

Despite the significant impact of hydrogen content on the equation of state (i.e. pressure at given volume), its influence on the self-diffusion coefficient of iron is minor(Fig.1 c, d). The self-diffusion coefficient of iron D_{Fe} remains almost unchanged with varying hydrogen content. However, the self-diffusion coefficient of hydrogen D_H shows some fluctuations, especially at low hydrogen doping levels, due to the lattice deformation induced by the small amounts of hydrogen. We also found that iron fluid at 6000 K at a volume of 1071 \AA^3 ($P=153\text{-}193$ GPa) has a larger self-diffusion coefficient than iron fluid at 6000 and 7000 K in a volume of 905 \AA^3 ($P=311\text{-}384$ GPa), indicating that the diffusivity is strongly dependent on both temperature and pressure. Higher temperatures increase the kinetic energy of atoms, resulting in more vigorous vibrations and greater lattice deformation. Larger volumes at lower pressure allow atoms to

move easier, enhancing diffusivity.

We obtained the shear viscosity from the the off-diagonal stress tensor σ autocorrelation function (SACF), $C(t)$, which decays rapidly when t is small ([19]. The SACF converge to 0 at $t=0.15$ ps (Fig. 2 a) and show little dependence on H content. We obtain the frequency dependent viscosity $\eta(\omega)$ and shear modulus $G(\omega)$ for the fluid from the Fourier transform of $C(t)$. The viscosity, $\eta(\omega)$, decreases monotonically with frequency, and $G(\omega)$ increases from zero and plateaus at high frequencies (Fig. 2 b). From these numerical Fourier transform integration of the original molecular dynamics (MD) data, we can derive the viscosity and shear modulus, corresponding to the zero-frequency viscosity η_0 and the infinite-frequency shear modulus G_∞ , respectively. We find that the viscosity of the Fe-H alloy at 6000 K and a volume of 1071 \AA^3 does not vary significantly with hydrogen doping levels of 0, 16, and 32 H atoms (corresponding to $P=153, 173,$ and 193 GPa). However, the shear modulus increases with higher hydrogen doping content. The shear modulus and viscosity increase a lot at higher pressure when we vary the volumes at 6000 K. Additionally, we compare the viscosity and shear modulus at different temperatures (Fig. 2 (c-d)). With increasing hydrogen content, the shear modulus increases significantly due to the rise in internal pressure caused by the hydrogen. The shear modulus of the Fe-H alloy slightly decreases with higher temperatures. In contrast, the viscosity is minimally affected by hydrogen doping but decreases with rising temperatures. We obtain a viscosity of $\sim 10.0 \text{ mPa} \cdot \text{s}$ for the Fe-H alloy under Earth’s outer core conditions, which is $\sim 20\%$ higher than previous results[19].

Besides the exact linear-response approach, the viscosity of liquid iron has also been approximately determined from diffusivity using the Stokes–Einstein relation, which is found to be valid under the high-pressure and high-temperature conditions of Earth’s outer core [30]. The chemical diffusivities of Fe and H increase linearly with hydrogen content (Fig. S1), leading to a linearly increasing Stokes–Einstein constant a (Eq. 7 in supplemental material[30]). For a fixed density, high temperatures enhance the average diffusivity of the Fe-H alloy but decrease the inverse $k_B T$. Thus we find that the Stokes–Einstein constant varies only slightly between 4000 and 6000 K, which verifying the validity of the Stokes–Einstein relation. The behavior of average diffusivities is also significantly dependent on the H content and lead to a sharply increasing Stokes–Einstein constant as H content varies.

Other than atomic transport properties calculations, we furthermore carry out simulations for electrical resistivity and thermal conductivity of Fe-H alloy, which are crucial for our understanding of the Earth’s core evolution. We sampled three configurations from Fe-H alloy FPMD simulations and computed electron-phonon (*e-ph*) scattering contributions to electrical and thermal conductivity by density functional theory (DFT) and both electron-phonon/electron-electron (*e-ph/e-e*)

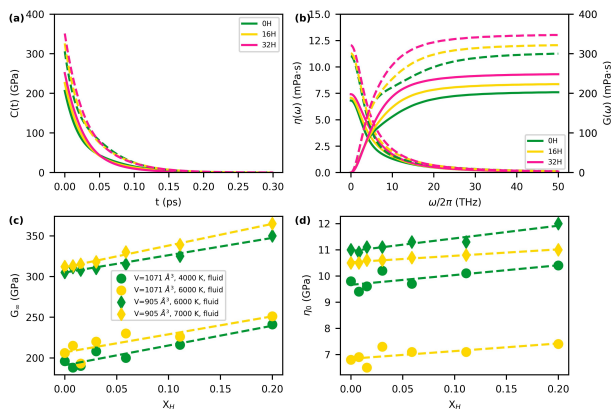


FIG. 2. **Viscosity of liquid iron-hydrogen alloy at Earth's core conditions.** **a** Stress autocorrelation functions (SACFs) of liquid iron-hydrogen alloy at 6000 K and $V=1071$ (solid), 905 (dash) \AA^3 by doping 0H (green, pure iron), 16H (yellow) and 32H (red). See Fig. 1a for the corresponding pressures. **b** Frequency-dependent viscosity ($\eta(\omega)$, lines decreasing to zero, corresponding to left y-axis) and shear modulus ($G(\omega)$, lines increasing, corresponding to right y-axis) of liquid iron at 6000 K and $V=1071$ (solid), 905 (dash) \AA^3 with various hydrogen doping content. Only the real parts of $\eta(\omega)$ and $G(\omega)$ are shown. **c** Infinite frequency shear modulus G_∞ and **d** zero frequency viscosity η_0 (green, lower T and yellow, higher T) at $V=1071$ (dot) and 905 (diamond) \AA^3 . The lines are linear fits to the points.

scattering contributions by dynamical mean field theory (DMFT) using a modified Spin-polarized Relativistic Korringa-Kohn-Rostoker (SPR-KKR) package[33, 34]. Strictly, the liquid does not have phonons; it is the liquid disorder that gives rise to resistivity from scattering in liquids.

We computed the electrical resistivity and thermal conductivity using the Green-Kubo method for MD snapshots (Fig.3). For pure iron (0H), we obtained electrical resistivity values of 68 ± 3 and $76 \pm 0.2 \mu\Omega \cdot \text{cm}$ for the *hcp* phase using DFT and DMFT calculations at outer core conditions (130 GPa and 4000 K). The corresponding thermal conductivity values are 127 ± 5 and $110 \pm 1 \text{ Wm}^{-1}\text{K}^{-1}$, consistent with previous FPMD+DFT/DMFT results[8]. The computed electrical resistivity of liquid iron is higher by $\sim 4 \mu\Omega \cdot \text{cm}$ and the thermal conductivity lower by $\sim 10 \text{ Wm}^{-1}\text{K}^{-1}$ compared to the *hcp* phase iron at 135 GPa and 4000 K. Heating iron to 6000 K and 153 GPa resulted in a saturation of electrical resistivity in liquid iron, while the thermal conductivity increased to $130 \pm 4 \text{ Wm}^{-1}\text{K}^{-1}$, approximately 20% lower than previous DFT results[35]. Matthiessen's rule is expected to be broken in the saturation region when the resistivity approaches the Ioffe-Regel limit, as this limit represents the minimum mean free path, essentially the nearest-neighbor distance[36–38]. For strongly correlated systems of Fe-H alloy at core conditions, resistivity can significantly exceed the Ioffe-Regel limit, corresponding to an extremely short mean free path.

For solid iron at the top of the inner core, we obtained electrical resistivity values of 59 ± 0.2 and $67 \pm 0.2 \mu\Omega \cdot \text{cm}$ for the *hcp* phase using DFT and DMFT calculations. The corresponding thermal conductivity values are 220 ± 5 and $183 \pm 1 \text{ Wm}^{-1}\text{K}^{-1}$. Upon heating from 6000 K to 7000 K at ~ 350 GPa, we again observe saturation of electrical resistivity in liquid iron, which was also reported in previous light elements impurity studies[11, 20, 21, 39]. From the solid phase to the liquid phase at 6000 K, the electrical resistivity increases by $\sim 6 \mu\Omega \cdot \text{cm}$, whereas the thermal conductivity decreases by $\sim 16\%$. In fluid iron, thermal conductivity increases with rising temperature.

Curiously, our analysis of the electronic density of states (DOS) of these molecular dynamics (MD) configurations at outer core conditions reveals that the DOS reaches its maximum at the Fermi level (Fig. S2). However, the DOS at the Fermi level decreases with increasing hydrogen (H) content, which in turn induces higher electrical resistivity in the Fe-H alloy. The error bars displayed are larger in solid iron phases compared to liquid phases due to the anisotropy of the solid. The electrical resistivity saturates at high temperatures regardless of H content, although impurities do increase the resistivity values (Fig. 3a). At outermost core conditions, a hydrogen content of 20 mol% (0.45 wt%) increases the electrical resistivity by $\sim 10\%$ compared to pure iron, according to density functional theory (DFT) calculations (solid orange line). Our dynamical mean-field theory (DMFT, simulation detail in supplemental materials[30]) results also show that electrical resistivity increases linearly with H content and are moderately higher than those obtained from DFT calculations.

The thermal conductivity decreases with H content (Fig. 3 b). At the innermost outer core conditions, 0.45 wt% H (solid deep blue) suppresses the thermal conductivity of *hcp* phase iron by $\sim 13\%$. DMFT calculations give smaller values than DFT for the thermal conductivity at core conditions. For example, the thermal conductivities of the solid *hcp* phase at inner core conditions (open blue circles) from DMFT calculations are $\sim 30 \text{ Wm}^{-1}\text{K}^{-1}$ lower than predicted by DFT for the same hydrogen content (solid blue circles). Similarly, for the solid phase at outermost outer core conditions, DMFT results (open light green circles) are about $\sim 15 \text{ Wm}^{-1}\text{K}^{-1}$ lower than those from DFT (solid light green circles). For fluid iron at outermost outer core conditions (solid orange), the effects of H is slightly weaker, especially for DMFT calculations. Unlike the saturation of electrical resistivity in liquid Fe-H alloys, the thermal conductivity keeps increasing with higher temperatures. We obtain thermal conductivity values of ~ 105 and $\sim 190 \text{ Wm}^{-1}\text{K}^{-1}$ for the outer and inner core with 0.45 wt% H content according to DFT calculations, which are respectively about $\sim 13\%$ and $\sim 8\%$ lower than the corresponding values in pure iron.

In some previous studies[6, 7], the thermal conductivity of iron under extreme conditions was obtained from

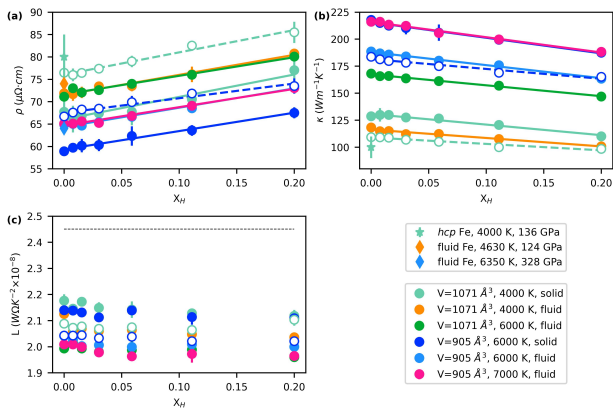


FIG. 3. **Electrical transport properties of Fe-H alloy at the Earth's core conditions.** **a** Electrical resistivity and **b** thermal conductivity evolution in two fixed volumes at different temperatures with doping H content. See Fig.1 a for the corresponding pressures. Six curves are divided into two sets: solid phase at 4000 K (light green), fluid phase at 4000 K (orange), fluid phase at 6000 K (green) in a larger volume ($V=1071 \text{ \AA}^3$); and solid phase at 6000 K (blue), fluid phase at 6000 K (light blue), fluid phase at 7000 K (magenta) in a smaller volume ($V=905 \text{ \AA}^3$). The error bars represent standard deviation from configurations sampling. DFT/DMFT results are marked with solid/open circles. We fit linear solid/dash curves for these discrete DFT/DMFT values that share the same volume, temperature, and state. The light green stars and orange/light blue diamonds are from computations in Ref[8] and Ref[40]. The ideal Lorenz number ($L_0=2.44 \times 10^{-8} \text{ W}\Omega\text{K}^{-2}$) is shown as the dotted horizontal line at the top.

the electrical resistivity by applying the Wiedemann-Franz law: $\kappa = LT\sigma$, where thermal and electrical conductivity (κ and σ) are associated by temperature T and Lorenz number L , with an ideal Lorenz number $L_0 = 2.44 \times 10^{-8} \text{ W}\Omega\text{K}^{-2}$. Based on our FPMD+DFT/DMFT results, we compute the Lorenz number L of the Fe-H alloy. The Lorenz number is estimated to be $\sim(1.95-2.2) \times 10^{-8} \text{ W}\Omega\text{K}^{-2}$ (Fig. 3c), which is $\sim(10-20)\%$ lower than the ideal value. Overall, we found that H impurities do not alter the Lorenz number significantly. The solid phases have larger value than that of fluid phases at same density of Fe-H alloy and the Lorenz number decreases with higher temperatures. We obtain a Lorenz number of 2.05 and $2.13 \times 10^{-8} \text{ W}\Omega\text{K}^{-2}$ for $\text{Fe}_{99.55}\text{H}_{0.45}$ alloy at the outermost and innermost outer core conditions of Earth. Our results give a Lorenz number of $2.19 \times 10^{-8} \text{ W}\Omega\text{K}^{-2}$ for pure hcp iron at outermost core condition of Earth's, which is consistent with previous DFT computations. [8].

The interest in determining the transport properties of iron and iron-light element alloys, such as thermal conductivity, is mainly driven by thermal evolution modeling. Directly measuring the thermal properties of these materials at planetary core conditions is challenging, and extrapolations from lower pressure and temperature conditions are not always accurate[7, 41]. Our calculations indicate a breakdown of the ideal Wiedemann-Franz law in Fe-H alloys, meaning thermal conductivity cannot be indirectly derived from electrical resistivity. Notably, we observed saturation of electrical resistivity in the liquid phase of Fe-H alloy under core conditions, while thermal conductivity increases with temperature. Assuming the Earth's core cools from an early fluid state, the fluid inner core would experience a $\sim 13\%$ decrease in thermal conductivity from 7000 K to 6000 K, followed by an increase upon crystallization.

Earth's outer core contains approximately 8 wt% light elements, such as silicon (Si), oxygen (O), sulfur (S), and carbon (C), along with about 5 wt% nickel (Ni)[42, 43]. Recent studies suggest that each weight percent of these light elements can reduce thermal conductivity by 2%–4% near core-mantle boundary (CMB) conditions, according to recent calculations and high-pressure experiments[20, 35, 44–46]. Our simulations have only included 0.45 wt% hydrogen (H) in iron, which can reduce thermal conductivity by 8-13% at the Earth's core conditions than that of the pure iron. The difference in thermal conductivity is significant but reasonable, because hydrogen has a much smaller mass than other light elements. The exact amount of hydrogen in the core is unknowable, but it has a rather minor effect on transport properties. Since such experiments are unavailable and exceedingly difficult, this is a fortunately result. We also find that melting has only a minor effect on electronic transport in high pressure iron. This is important as there are no experiments on resistivity or thermal conductivity in molten iron.

ACKNOWLEDGMENTS

This work is supported by US National Science Foundation CSEDI grant EAR-1901813 and Carnegie Institution for Science. We gratefully acknowledges supercomputer support from Resnick High Performance Computing Center. The authors gratefully acknowledge the Gauss Centre for Supercomputing e.V. (www.gauss-centre.eu) for funding this project by providing computing time on the GCS Supercomputer SuperMUC-NG at Leibniz Supercomputing Centre (www.lrz.de).

- [1] J.-P. Poirier, Light elements in the Earth's outer core: A critical review, *Physics of the Earth and Planetary Interiors* **85**, 319 (1994).
- [2] K. Hirose, B. Wood, and L. Vočadlo, Light elements in

- the Earth's core, *Nat Rev Earth Environ* **2**, 645 (2021).
- [3] G. A. de Wijs, G. Kresse, L. Vočadlo, D. Dobson, D. Alfè, M. J. Gillan, and G. D. Price, The viscosity of liquid iron at the physical conditions of the Earth's core, *Nature*

- 392**, 805 (1998).
- [4] M. Pozzo, C. Davies, D. Gubbins, and D. Alfè, Thermal and electrical conductivity of iron at Earth’s core conditions, *Nature* **485**, 355 (2012).
- [5] Z. Konôpková, R. S. McWilliams, N. Gómez-Pérez, and A. F. Goncharov, Direct measurement of thermal conductivity in solid iron at planetary core conditions, *Nature* **534**, 99 (2016).
- [6] H. Gomi and K. Hirose, Electrical resistivity and thermal conductivity of hcp Fe–Ni alloys under high pressure: Implications for thermal convection in the Earth’s core, *Physics of the Earth and Planetary Interiors Transport Properties of the Earth’s Core*, **247**, 2 (2015).
- [7] K. Ohta, Y. Kuwayama, K. Hirose, K. Shimizu, and Y. Ohishi, Experimental determination of the electrical resistivity of iron at Earth’s core conditions, *Nature* **534**, 95 (2016).
- [8] Y. Zhang, M. Hou, G. Liu, C. Zhang, V. B. Prakapenka, E. Greenberg, Y. Fei, R. E. Cohen, and J.-F. Lin, Reconciliation of Experiments and Theory on Transport Properties of Iron and the Geodynamo, *Phys. Rev. Lett.* **125**, 078501 (2020).
- [9] E. Edmund, G. Morard, M. A. Baron, A. Rivoldini, S. Yokoo, S. Boccato, K. Hirose, A. Pakhomova, and D. Antonangeli, The Fe-FeSi phase diagram at Mercury’s core conditions, *Nat Commun* **13**, 387 (2022).
- [10] Y. Zhang, K. Luo, M. Hou, P. Driscoll, N. P. Salke, J. Minár, V. B. Prakapenka, E. Greenberg, R. J. Hemley, R. E. Cohen, and J.-F. Lin, Thermal conductivity of Fe-Si alloys and thermal stratification in Earth’s core, *Proceedings of the National Academy of Sciences* **119**, e2119001119 (2022).
- [11] M. Pozzo and D. Alfè, Saturation of electrical resistivity of solid iron at Earth’s core conditions, *SpringerPlus* **5**, 256 (2016).
- [12] M. Pozzo, C. Davies, D. Gubbins, and D. Alfè, Thermal and electrical conductivity of solid iron and iron–silicon mixtures at Earth’s core conditions, *Earth and Planetary Science Letters* **393**, 159 (2014).
- [13] X. Sha and R. E. Cohen, First-principles studies of electrical resistivity of iron under pressure, *Journal of Physics: Condensed Matter* **23**, 075401 (2011).
- [14] J. Badro, J. Siebert, and F. Nimmo, An early geodynamo driven by exsolution of mantle components from Earth’s core, *Nature* **536**, 326 (2016).
- [15] J. G. O’Rourke and D. J. Stevenson, Powering Earth’s dynamo with magnesium precipitation from the core, *Nature* **529**, 387 (2016).
- [16] J. Xu, P. Zhang, K. Haule, J. Minar, S. Wimmer, H. Ebert, and R. E. Cohen, Thermal Conductivity and Electrical Resistivity of Solid Iron at Earth’s Core Conditions from First Principles, *Phys. Rev. Lett.* **121**, 096601 (2018).
- [17] M. Greff-Lefftz and H. Legros, Core-mantle coupling and viscoelastic deformations, *Physics of the Earth and Planetary Interiors Structure and Dynamics of the Earth’s Inner and Outer Cores*, **90**, 115 (1995).
- [18] H. Ichikawa and T. Tsuchiya, Atomic transport property of Fe–O liquid alloys in the Earth’s outer core P , T condition, *Physics of the Earth and Planetary Interiors Transport Properties of the Earth’s Core*, **247**, 27 (2015).
- [19] Q. Li, T. Sun, Y.-g. Zhang, J.-W. Xian, and L. Vočadlo, Atomic transport properties of liquid iron at conditions of planetary cores, *The Journal of Chemical Physics* **155**, 194505 (2021).
- [20] F. Wagle, G. Steinle-Neumann, and N. de Koker, Resistivity saturation in liquid iron–light-element alloys at conditions of planetary cores from first principles computations, *Comptes Rendus. Géoscience* **351**, 154 (2019).
- [21] H. Inoue, S. Suehiro, K. Ohta, K. Hirose, and Y. Ohishi, Resistivity saturation of hcp Fe-Si alloys in an internally heated diamond anvil cell: A key to assessing the Earth’s core conductivity, *Earth and Planetary Science Letters* **543**, 116357 (2020).
- [22] M. Hou, Y. He, B. G. Jang, S. Sun, Y. Zhuang, L. Deng, R. Tang, J. Chen, F. Ke, Y. Meng, V. B. Prakapenka, B. Chen, J. H. Shim, J. Liu, D. Y. Kim, Q. Hu, C. J. Pickard, R. J. Needs, and H.-K. Mao, Superionic iron oxide–hydroxide in Earth’s deep mantle, *Nat. Geosci.* **14**, 174 (2021).
- [23] W. Wang, Y. Li, J. P. Brodholt, L. Vočadlo, M. J. Walter, and Z. Wu, Strong shear softening induced by superionic hydrogen in Earth’s inner core, *Earth and Planetary Science Letters* **568**, 117014 (2021).
- [24] J. Zhang, H. Liu, Y. Ma, and C. Chen, Direct H-He chemical association in superionic FeO2H2He at deep-Earth conditions, *National Science Review* **9**, nwab168 (2022).
- [25] Y. He, S. Sun, D. Y. Kim, B. G. Jang, H. Li, and H.-k. Mao, Superionic iron alloys and their seismic velocities in Earth’s inner core, *Nature* **602**, 258 (2022).
- [26] H. Yang, J. M. R. Muir, and F. Zhang, Iron Hydride in the Earth’s Inner Core and Its Geophysical Implications, *Geochemistry, Geophysics, Geosystems* **23**, e2022GC010620 (2022).
- [27] I. Park, Y. He, H.-k. Mao, J. H. Shim, and D. Y. Kim, Electride Formation of HCP-Iron at High Pressure: Unraveling the Origin of the Superionic State of Iron-Rich Compounds in Rocky Planets, *Advanced Science* **11**, 2308177 (2024).
- [28] G. Kresse and J. Furthmüller, Efficient iterative schemes for ab initio total-energy calculations using a plane-wave basis set, *Phys. Rev. B* **54**, 11169 (1996).
- [29] P. Giannozzi, S. Baroni, N. Bonini, M. Calandra, R. Car, C. Cavazzoni, D. Ceresoli, G. L. Chiarotti, M. Cococcioni, I. Dabo, A. D. Corso, S. de Gironcoli, S. Fabris, G. Fratesi, R. Gebauer, U. Gerstmann, C. Gougoussis, A. Kokalj, M. Lazzeri, L. Martin-Samos, N. Marzari, F. Mauri, R. Mazzarello, S. Paolini, A. Pasquarello, L. Paulatto, C. Sbraccia, S. Scandolo, G. Sclauzero, A. P. Seitsonen, A. Smogunov, P. Umari, and R. M. Wentzcovitch, QUANTUM ESPRESSO: A modular and open-source software project for quantum simulations of materials, *J. Phys.: Condens. Matter* **21**, 395502 (2009).
- [30] See supplemental material at url-will-be-inserted-by-publisher for the simulation detail and other figures., .
- [31] C. Cavazzoni, G. L. Chiarotti, S. Scandolo, E. Tosatti, M. Bernasconi, and M. Parrinello, Superionic and Metallic States of Water and Ammonia at Giant Planet Conditions, *Science* **283**, 44 (1999).
- [32] C. Liu, H. Gao, Y. Wang, R. J. Needs, C. J. Pickard, J. Sun, H.-T. Wang, and D. Xing, Multiple superionic states in helium–water compounds, *Nature Physics* **15**, 1065 (2019).
- [33] H. Ebert, D. Ködderitzsch, and J. Minár, Calculating condensed matter properties using the KKR-Green’s function method—recent developments and applications, *Rep. Prog. Phys.* **74**, 096501 (2011).
- [34] J. Minár, Correlation effects in transition metals and

- their alloys studied using the fully self-consistent KKR-based LSDA + DMFT scheme, *J. Phys.: Condens. Matter* **23**, 253201 (2011).
- [35] N. de Koker, G. Steinle-Neumann, and V. Vlček, Electrical resistivity and thermal conductivity of liquid Fe alloys at high P and T, and heat flux in Earth's core, *Proceedings of the National Academy of Sciences* **109**, 4070 (2012).
- [36] M. Gurvitch, Ioffe-Regel criterion and resistivity of metals, *Phys. Rev. B* **24**, 7404 (1981).
- [37] O. Gunnarsson, M. Calandra, and J. E. Han, Colloquium: Saturation of electrical resistivity, *Rev. Mod. Phys.* **75**, 1085 (2003).
- [38] F. Rizzo, E. Cappelluti, and L. Pietronero, Transport properties in correlated systems: An analytical model, *Phys. Rev. B* **72**, 155113 (2005).
- [39] H. Gomi, K. Hirose, H. Akai, and Y. Fei, Electrical resistivity of substitutionally disordered hcp Fe–Si and Fe–Ni alloys: Chemically-induced resistivity saturation in the Earth's core, *Earth and Planetary Science Letters* **451**, 51 (2016).
- [40] M. Pozzo, C. Davies, D. Gubbins, and D. Alfè, Transport properties for liquid silicon-oxygen-iron mixtures at Earth's core conditions, *Phys. Rev. B* **87**, 014110 (2013).
- [41] S. Suehiro, T. Wakamatsu, K. Ohta, K. Hirose, and Y. Ohishi, High-temperature electrical resistivity measurements of hcp iron to Mbar pressure in an internally resistive heated diamond anvil cell, *High Pressure Research* **39**, 579 (2019).
- [42] J. Li and Y. Fei, 2.14 - Experimental Constraints on Core Composition, in *Treatise on Geochemistry*, edited by H. D. Holland and K. K. Turekian (Pergamon, Oxford, 2007) pp. 1–31.
- [43] Y. Fei, C. Murphy, Y. Shibazaki, A. Shahar, and H. Huang, Thermal equation of state of hcp-iron: Constraint on the density deficit of Earth's solid inner core, *Geophysical Research Letters* **43**, 6837 (2016).
- [44] C. T. Seagle, E. Cottrell, Y. Fei, D. R. Hummer, and V. B. Prakapenka, Electrical and thermal transport properties of iron and iron-silicon alloy at high pressure, *Geophysical Research Letters* **40**, 5377 (2013).
- [45] S. Suehiro, K. Ohta, K. Hirose, G. Morard, and Y. Ohishi, The influence of sulfur on the electrical resistivity of hcp iron: Implications for the core conductivity of Mars and Earth, *Geophysical Research Letters* **44**, 8254 (2017).
- [46] Q. Williams, The Thermal Conductivity of Earth's Core: A Key Geophysical Parameter's Constraints and Uncertainties, *Annual Review of Earth and Planetary Sciences* **46**, 47 (2018).
- [47] J. P. Perdew, K. Burke, and M. Ernzerhof, Generalized Gradient Approximation Made Simple, *Phys. Rev. Lett.* **77**, 3865 (1996).
- [48] K. F. Garrity, J. W. Bennett, K. M. Rabe, and D. Vanderbilt, Pseudopotentials for high-throughput dft calculations, *Computational Materials Science* **81**, 446 (2014).
- [49] Y. Liu and D. Block, Stokes-Einstein relation for binary mixtures, *Computer Physics Communications* **300**, 109184 (2024).
- [50] P. E. Blöchl, Projector augmented-wave method, *Phys. Rev. B* **50**, 17953 (1994).

Supplementary Materials for **Electrical resistivity, thermal conductivity, and viscosity of Fe-H alloys at Earth's core conditions**

I. SIMULATION DETAILS

For pressure estimation and configuration sampling, first-principles molecular dynamics (FPMD) simulations were conducted using Quantum ESPRESSO[29]. The Perdew–Burke–Ernzerhof (PBE)[47] generalized gradient approximation was employed for the exchange–correlation functional. Scalar-relativistic Garrity–Bennett–Rabe–Vanderbilt (GBRV) ultrasoft pseudopotentials[48] for Fe and H were utilized, with a plane wave cutoff energy set at 40 Ry. Simulations were performed in the NVT ensemble with the ionic temperature regulated by a stochastic-velocity rescaling thermostat and electronic temperatures managed using the Fermi–Dirac smearing function. A periodic hexagonal supercell containing 128 iron atoms was doped with varying amounts of hydrogen (0, 1, 2, 4, 8, 16, 32 H atoms, equal to 0-0.45 wt%) at interstitial sites. At $V=1071 \text{ \AA}^3$, simulations were conducted at 4000 K to represent the solid/fluid iron phase and at 6000 K for the fluid iron phase. At $V=905 \text{ \AA}^3$, simulations were conducted at 6000 K to represent the solid/fluid iron phase and at 7000 K for the fluid iron phase. We fixed the c/a ratio to 1.615. The Brillouin zone was sampled at the Γ -point, with an FPMD step of 1 fs and total simulation times exceeding 10 ps to ensure equilibrium. Bands with occupations larger than 10^{-5} were included. Macroscopic quantities such as temperature and pressure were averaged over 3000 equilibrium steps.

The self-diffusion coefficient D is derived from the mean square displacement $r^2(t)$ according to the following equations:

$$D = r^2(t)/6t \quad (1)$$

$$r^2(t) = \left\langle [r_i(t+t_0) - r_i(t_0)]^2 \right\rangle_{i,t_0} \quad (2)$$

For viscosity simulations, first-principles molecular dynamics (FPMD) simulations were performed with the Vienna ab initio simulation package (VASP)[28], using the projector augmented-wave (PAW) method. We used $3d^7$ and $1s^1$ as valence electrons for Fe and H, and used the generalized gradient approximation (GGA) in the Perdew–Burke–Ernzerhof (PBE)[47, 50] exchange correlation functional.

We adopted the canonical NVT ensemble using a Nose–Hoover thermostat to perform AIMD simulations in a supercell with 128 atoms Fe and doping H number of 0, 1, 2, 4, 8, 16, 32, with Γ -centered k-points sampling and a cutoff energy of 600 eV were adopted to ensure energy convergence of better than 10^{-5} . At $V=1071 \text{ \AA}^3$, simulations were conducted at 4000 K to represent the solid/fluid iron phase and at 6000 K for the fluid iron phase. At $V=905 \text{ \AA}^3$, simulations were conducted at 6000 K to represent the solid/fluid iron phase and at 7000 K for the fluid iron phase. We fixed the c/a ratio to 1.615. Each simulation lasts for 12 ps with a time step of 1 fs, and we allowed the first 2 ps for thermalization. From these fluid equilibrium MD trajectories, we calculated the viscosity $\eta(t)$ of liquid Fe-H alloy from the linear-response Green–Kubo formula by integrating the off-diagonal stress tensor σ autocorrelation function (SACF) $C(t)$ from 0 to t ,

$$C(t) = \frac{V}{k_B T} \langle \sigma(t)\sigma(t+t_0) \rangle_{t_0} \quad (3)$$

$$\eta(t) = \int_0^t C(t_0) dt_0 \quad (4)$$

The final viscosity η is taken for $t \rightarrow \infty$. For SACF, we used a cutoff of 2 ps and then fitted the data with the two exponentials. This reproduces well the long time behavior of $C(t)$ beyond the ballistic region.[19]

$$C(t) = G_\infty \left[(1 - \alpha) \text{sech}^2(t/\tau_1) + \alpha e^{-t/\tau_2} \right] \quad (5)$$

We obtain the frequency dependent viscosity $\eta(\omega)$ and shear modulus $G(\omega)$ for the fluid from the Fourier transform of $C(t)$.

$$\eta(\omega) = \int_0^\infty C(t) e^{-i\omega t} dt \quad (6)$$

$$G(\omega) = i\omega\eta(\omega) \quad (7)$$

where σ represents the three independent components of the off-diagonal stress tensor: $\sigma_{xy}, \sigma_{yz}, \sigma_{zx}$, and V, k_B, T are the cell volume, the Boltzmann constant, and the temperature, respectively.

The Stokes–Einstein relation between viscosity and diffusivity is given by:

$$\frac{D\eta}{\rho^{1/3}k_B T} = a, \quad (8)$$

where $\rho = N/V$ is the number density, and a is the Stokes-Einstein constant. For binary system of Fe-H alloy, we firstly average the diffusion constants of Fe and H [49]:

$$D_{avg} = \frac{N_{Fe}D_{Fe} + N_H D_H}{N_{Fe} + D_h}. \quad (9)$$

We used a modified Spin-polarized Relativistic Korringa-Kohn-Rostoker (SPR-KKR) package[33, 34] for the transport calculations for Fe-H alloy randomly sampled snapshots from AIMD simulations. For each configuration, the calculations commenced with a self-consistent-field (SCF) calculation using density functional theory (DFT). We used a maximum angular momentum lmax of 3 (nl=4) with 27 k-points. We tested the choice of nl and find that higher nl gives slightly lower electrical resistivity and Lorenz number and slightly higher thermal conductivity (Fig.S3). Subsequently, transport calculations were performed using the converged potentials obtained from the SCF step, employing the Kubo-Greenwood method with a maximum angular momentum lmax of 3 on 64 k-points and energies $[-5 k_B T, 5 k_B T]$ around the chemical potential. The values for electrical resistivity (ρ , equal to the inverse of electrical conductivity $1/\sigma$) and thermal conductivity (κ) are expressed as follows:

$$\sigma = \mathcal{L}_{11} \quad (10)$$

$$\kappa = \frac{1}{eT} \left(\mathcal{L}_{22} - \frac{\mathcal{L}_{12}^2}{\mathcal{L}_{11}} \right) \quad (11)$$

and \mathcal{L}_{ij} is given by:

$$\mathcal{L}_{ij} = (-1)^{(i+j)} \int d\varepsilon \sigma_{\mu\nu}(\varepsilon - \mu)^{(i+j-2)} \left(-\frac{\delta f_T(\varepsilon)}{\delta \varepsilon} \right) \quad (12)$$

At a given temperature T , $f_T(\varepsilon)$ represents the Fermi-Dirac distribution function. The energy-dependent conductivity is given by the Kubo expression :

$$\sigma_{\mu\nu} \propto \text{Tr} \left\langle \hat{j}_\mu \text{Im} G^+ \hat{j}_\nu \text{Im} G^+ \right\rangle \quad (13)$$

where \hat{j}_μ is the current density operator, and $\text{Im} G^+$ is the imaginary part of retarded Green function. For transport calculations, We used a maximum angular momentum l_{max} of 4 and energies window of $\pm 5 k_B T$ around the chemical potential with a uniform k-point sampling of $4 \times 4 \times 4$.

We also calculate the electrical resistivity due to electron-electron scattering by fully relativistic KKR-DMFT implemented in the SPR-KKR package. We used the SPTF (spin-polarized T matrix + FLEX (fluctuation exchange)) impurity solver with a Hubbard parameter $U=4.0$ eV and the $J=0.943$ eV. The analytical continuations of the bath Green's function and electronic self-energy are done using the Padé approximation. For SCF step, we used a maximum angular momentum lmax of 3 with 2 k-points. Subsequently, transport calculations were performed using the converged potentials obtained from the SCF step, employing the Kubo-Greenwood method with a maximum angular momentum lmax of 3 on 64 k-points and energies $[-5 k_B T, 5 k_B T]$ around the chemical potential. Tests show that our results are converged with respect to all parameters.

II. SUPPLEMENTAL FIGURES

We show the Stokes-Einstein relation and Density of states (DOS) in figures below:

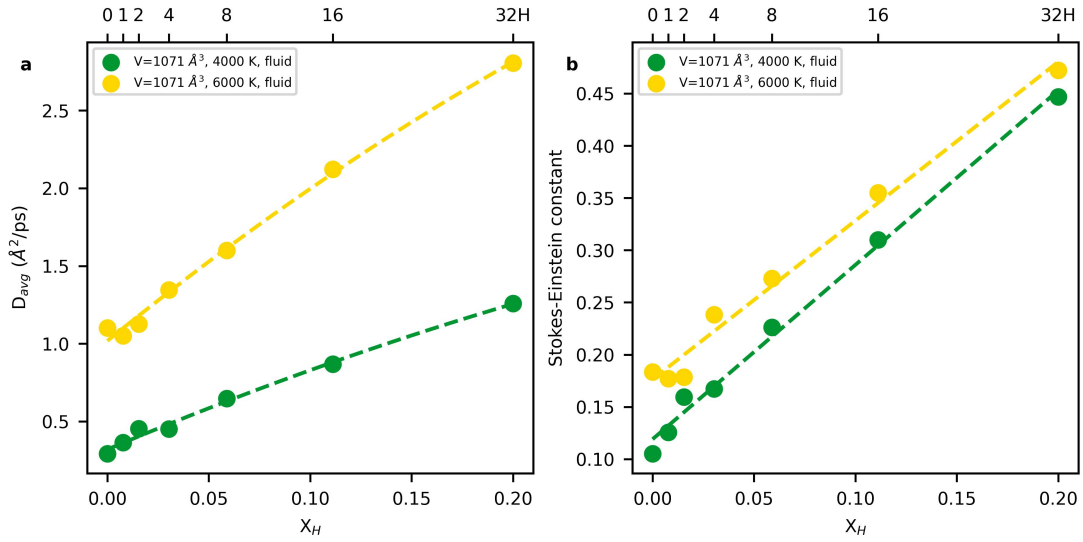


FIG. S1. Stokes-Einstein relation at the the fixed volume of 1071 \AA^3 with increasing doping H content for 4000 K fluid phase and 6000 K fluid phase. **a** Composition averaged self-diffusion coefficient ($D_{avg} = (D_{Fe}N_{Fe} + D_H N_H)/(N_{Fe} + N_H)$) and **b** Stokes-Einstein dimensionless constant a ($a = D\eta/(\rho^{1/3}k_B T)$) as a function of the doping H content.

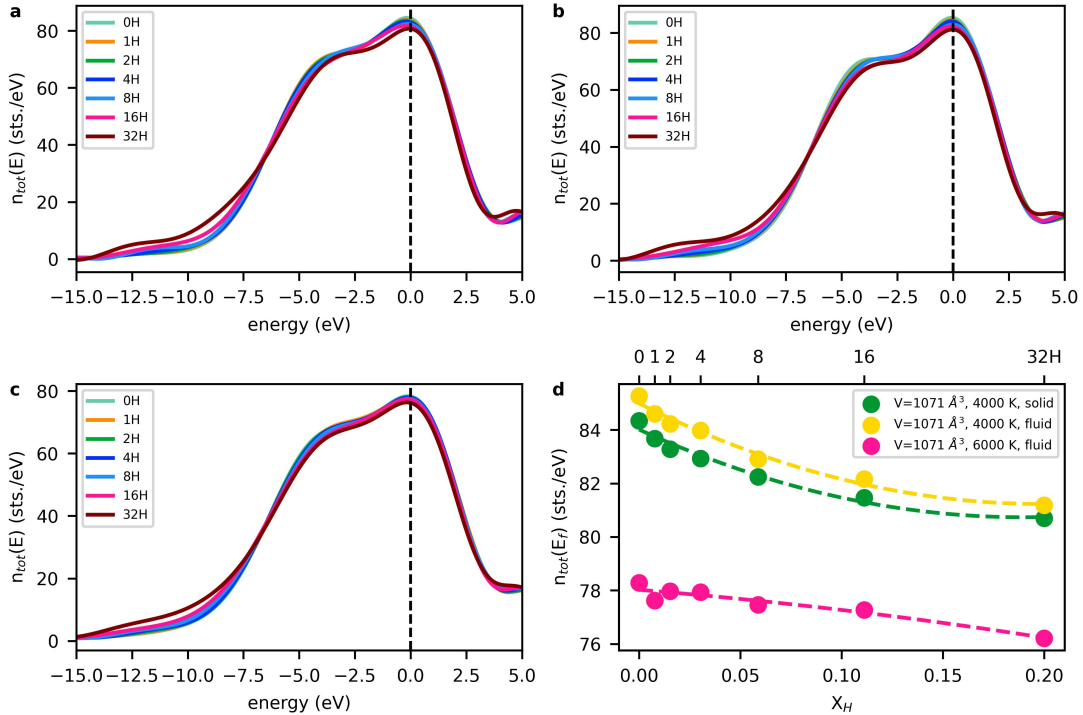


FIG. S2. Density of states (DOS) at the the fixed volume of 1071 \AA^3 with increasing doping H content for a 4000 K solid phase, **b** 4000 K fluid phase, and **c** 6000 K fluid phase. The energy windows are rescaled with $E_{Fermi}=0$ by dash black line. **d** Intensity of DOS at Fermi surface with increasing doping H content.

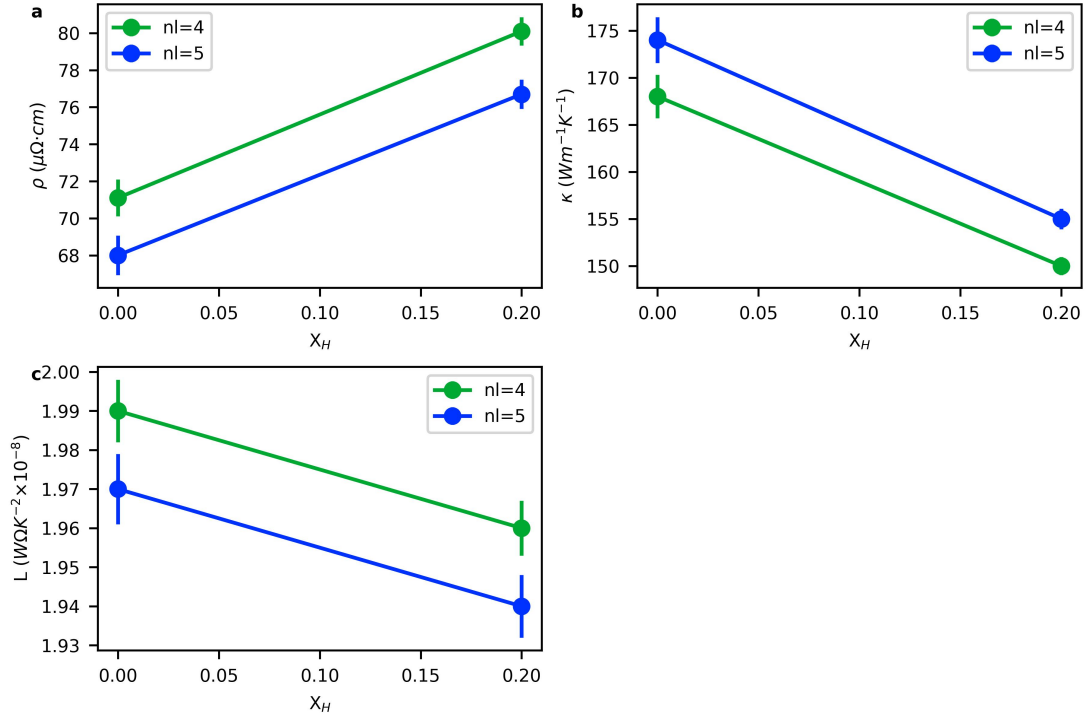


FIG. S3. Electrical transport properties of Fe-H alloy at the the fixed volume of 1071 Å³ for different angular momentum cutoffs in KKR. **a** Electrical resistivity, **b** thermal conductivity and **c** Lorenz number evolution with different maximum angular momentum l_{max} of 3 and 4, corresponding to $nl=4$ (green) and $nl=5$ (blue).